JOURNAL OF MATERIALS SCIENCE 22 (1987) 2799–2810

Microsegregation and eutectic ferrite-to-austenite transformation in primary austenite solidified CF-8M weld metals

N. LEWIS
General Electric Corporate Research and Development, Schenectady, New York 12301, USA
M. J. CIESLAK
Org. 1833-Process Metallurgy, Sandia National Laboratories, Albuquerque, New Mexico 87185, USA
W. F. SAVAGE
Materials Engineering Department, Rensselaer Polytechnic Institute, Troy, New York 12181, USA

Solidification and microsegregation studies were performed on alloy CF-8M weld metal which solidified via the primary austenite/eutectic ferrite mode. All of the major alloying elements (chromium, nickel, molybdenum) were observed to segregate to interdendritic areas upon solidification. Electron microprobe analysis revealed a substantial chromium and molybdenum enrichment of the eutectic ferrite relative to the austenite dendrites even in structures water-quenched from the solidus temperature. Scanning transmission electron microscopy/energy dispersive spectrometry (STEM/EDS) profiles taken within the eutectic ferrite phase revealed a similar pattern of major element distribution as has been observed by other investigators in residual primary delta ferrite dendrites. Within the eutectic ferrite, the highest chromium and molybdenum content and the lowest nickel content was found at the eutectic ferrite/austenite boundary. STEM/EDS analyses of *in situ* water-quenched weld microstructures revealed that compositional modification of the eutectic ferrite had occurred upon cooling from the solidus. In particular, the chromium concentration of the eutectic-ferrite was observed to increase by approximately 3 wt% in the temperature range ~1300 to ~750° C. In the same temperature range, the nickel content of the eutectic-ferrite decreased by approximately 4 wt% and the molybdenum content increased within the same phase by approximately 1 wt%. The transformation of eutectic ferrite to austenite as the weld metal cools to room temperature is consistent with a volume diffusion-control mechanism.

1. Introduction

CF-8M is an austenitic stainless steel casting alloy similar in composition to 316 stainless steel, containing chromium, nickel and molybdenum as the primary alloying components. The as-cast microstructure is typically austenitic, with 0 to 20% ferrite distributed throughout the matrix [1]. The weldability and subsequent transformations have been shown to be intimately related to the solidification behaviour and associated segregation phenomenon in this alloy system [2–6].

Several modes of solidification are possible within the CF-8M range of composition. Ferritic (F) solidification occurs when all liquid solidifies as delta ferrite. Ferritic–austenitic (F–A) solidification initiates with delta ferrite crystallizing as the primary phase and austenite subsequently solidifying on the existing ferrite via an eutectic/peritectic mechanism. Austenitic–ferritic (A–F) solidification occurs when austenite is the first phase to crystallize from the liquid, with eutectic ferrite solidifying in interdendritic volumes. Austenitic solidification (A) occurs when the alloy solidifies completely to austenite. In general, the ferrite phase is thermally unstable as the weld metal cools and transforms to austenite and possibly one of several intermetallic compounds, such as chi phase [2, 6–9].

From the literature, there is general agreement that the balance between ferrite stabilizers (chromium, molybdenum, silicon, niobium, titanium, tungsten, tantalum, vanadium, aluminium) and austenite stabilizers (nickel, manganese, carbon, nitrogen, copper, cobalt) is the primary factor controlling the solidification behaviour of stainless steel castings and arc welds [2–27]. Chromium and nickel equivalents, which are empirical measures of the relative ferrite and austenite promoting ability of the various alloying elements, have been developed to predict the room-temperature microstructure [9, 14, 26, 27] solidification mode [13–15] in austenitic stainless steel arc welds.

In this study, it was desired to investigate the

0022–2461/87 $03.00 + .12

TABLE I Chemical analysis*

Element	Heat 1	Heat 2
C	0.04	0.08
Mn	0.21	0.60
Si	0.38	1.05
Cr	19.55	18.32
Ni	15.38	13.20
Mo	2.88	2.26
S	0.025	0.016
P	0.036	0.035
N	0.04	0.04
Ferrite (vol %)	2.0	0.2

*All values in wt %, balance iron.

TABLE II Welding parameters

Electrode Composition Tungsten + 2% thoria
Electrode Conical, 90° apex angle
Electrode Extension from Collet 10.2 mm
Electrode diameter 3.2 mm
Travel speed 1.7 mm $\sec^{-1}$
Arc length 2.4 mm (measured cold)
Voltage 12 ± 0.5 V
Current (electrode negative) 250 ± 5 A
Shielding gas flow rate 0.32 litre $\sec^{-1}$ Ar

solidification and segregation patterns associated with autogenous gas-tungsten-arc (GTA) welding of alloys which solidified via the A–F sequence and to determine the effect of subsequent weld metal cooling on the microstructural features of specific CF-8M welds which had a well-documented history of weldability [3–5]. Alloys which solidified in the A–F mode were of particular interest for several reasons. The A–F solidification mode represents the cross-over region between alloys which are generally hot-crack resistant (F–A) and those prone to hot-cracking (A). CF-8M alloys solidifying by the A–F mode have been shown to precipitate chi phase at eutectic ferrite/austenite interfaces during sub-solidus cooling [2, 6]. The specifics of alloying element distribution during the transformation of eutectic ferrite to austenite have not been well documented. Finally, A–F alloys representative of commercial melting practice have not been as vigorously investigated as the corresponding F–A or A alloys.

2. Materials and procedures

The alloys used in this investigation were produced by member foundries of the Steel Founders' Society of America and represent results of normal foundry melt practice. Two heats of CF-8M, both of which solidified via the A–F sequence when GTA welded using 100% argon as the shielding gas, were studied. The composition of each alloy was determined by wet chemical analysis and is given in Table I. Each alloy was cast as a 305 mm long keel-block and was subsequently solution annealed at 1066° C for 1 h and water quenched. Weld specimens 305 mm × 51 mm × 13 mm were machined from these castings as described earlier [5]. The volume per cent ferrite was determined for all solution-treated castings using the point-count technique [28]. These data are also presented in Table I.

A high-pressure, water-spray quench technique, described by Arata *et al.* [7] was used to study the elemental segregation pattern within the weld microstructure. This procedure employed a linear GTA bead-on-plate weld. The welding parameters used are listed in Table II and are representative of conditions used in welding stainless steel castings. Prior to welding, all specimens were thoroughly cleaned with acetone and demagnetized. After a steady state pool geometry had been established (≈ 25 mm), a high-pressure water spray was applied from the front of the moving pool to extinguish the arc, decant the weld pool, and quench the trailing edge of the weld. The experimental set-up is shown schematically in Fig. 1. Fig. 2 shows an example of a water-quenched weld specimen. The solid–liquid interface structure at the trailing edge of the weld pool was cooled rapidly to room temperature in order to minimize the effect of solid state diffusion on solidification segregation. Areas in the weld metal back from the solid–liquid interface were also quenched from their respective temperatures. The effect of the quenching operation was to "freeze-in" the entire thermal history of the weld for subsequent analysis.

After the quenching operation, the decanted region and a portion of the trailing weld were removed with a water-cooled cut-off wheel. The section removed for observation is shown schematically in Fig. 1. Specimens for optical and electron microscopy, and microprobe analysis were made from these sections. Optical microscopy and scanning electron microscopy (SEM)

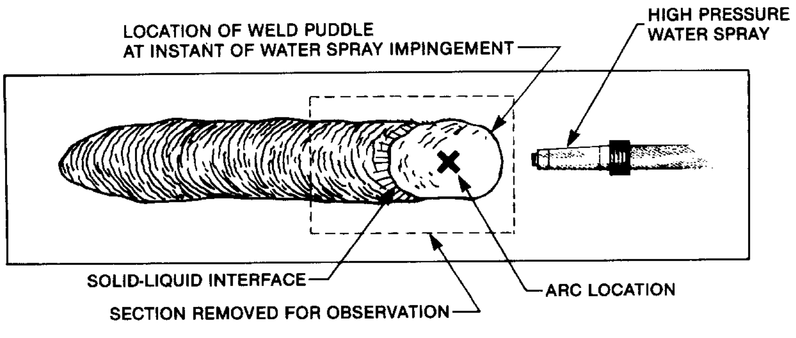

TOP SURFACE OF WELD SHOWING LOCATION
OF ARC, WELD PUDDLE AND SOLID-LIQUID
INTERFACE AT INSTANT OF QUENCHING

Figure 1 Schematic view of water quench experiment showing position of metallographic samples.

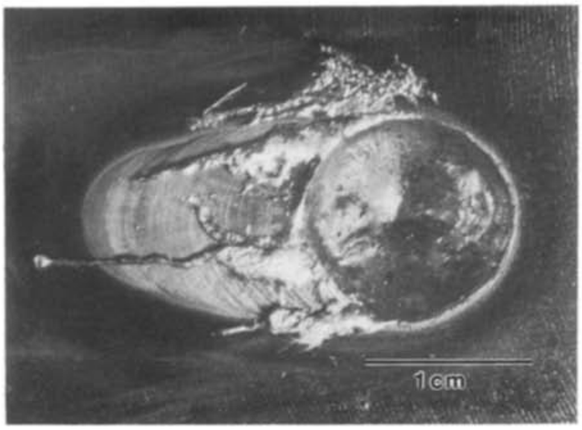

Figure 2 Macrophotograph showing representative water-spray-quench specimen.

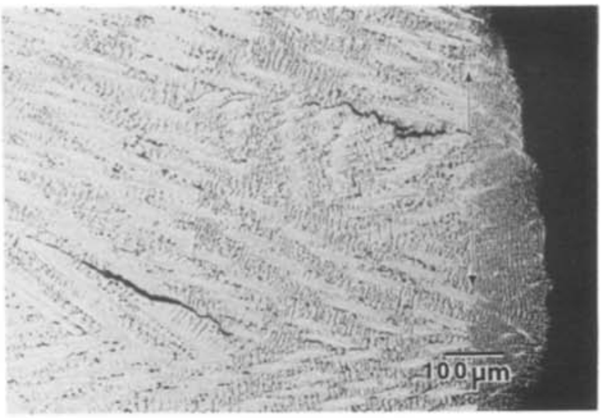

Figure 4 Optical micrograph of weld microstructure at the quench interface (arrows), Heat 2.

were performed after etching metallographic samples in a mixed acid etch ($H_2O:HCl:HNO_3$, 1 : 1 : 1). The samples were then repolished and very lightly etched to reveal the substructure for subsequent electron microprobe analysis.

SEM and electron microprobe analyses were performed with an automated Cameca MBX microprobe utilizing crystal diffracting spectrometers for X-ray detection. The characteristic $K\alpha$ X-ray lines were used for all elements analysed except molybdenum, where the $L\alpha$ X-ray line was used. Point counts were obtained for each element at times of 20 sec or more.

The microprobe analysis was performed with a regulated beam current of 30×10^{-8} A with an accelerating potential of 15 keV. These operating conditions were chosen to minimize the electron beam diameter and maximize spatial resolution of the emitted X-rays while still maintaining adequate X-ray counting rates. For the elements studied in this investigation, the X-ray spatial resolution was always less than 1 μm. Analytical sensitivities based on counting statistics were typically 2% relative for chromium, iron, nickel and molybdenum for a 95% confidence level. The raw data were reduced to weight per cent chemistry using a standard ZAF computer algorithm [29].

Specimens for scanning transmission electron microscopy (STEM)/energy dispersive X-ray spectroscopy (EDS) analysis were taken at predetermined distances ($\approx$ 1.0, 4.5, and 20.0 mm back from the quench interface) from longitudinal slices obtained along the weld centreline beginning at the quench interface. Each specimen analysed represents a different thermal history with specimens taken close to the quench interface retaining the microstructure and segregation pattern of higher temperatures. Samples were prepared by jet electropolishing using a solution of 20% perchloric acid in methanol at 25 V, 10 to 20 mA. An Hitachi H-600-1 analytical electron microscope operating at 100 keV was used. Microchemical analyses of regions of the specimen were performed by energy dispersive X-ray spectroscopy using a focused electron probe of 10 nm gaussian spot size. Reduction of X-ray intensity data to weight percentages was accomplished using the Cliff–Lorimer technique [30]. The Cr$K\alpha$, Fe$K\alpha$, Ni$K\alpha$, and Mo$K\alpha$ X-ray lines were used. The thin foil conditions present eliminated the need for an absorption correction [31]. The error bars for the STEM/EDS profiles are for 2σ values and are based upon errors in the k-factors and the X-ray counting statistics.

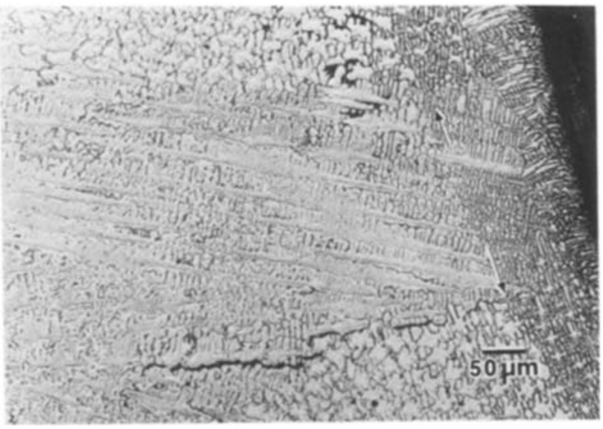

Figure 3 Optical micrograph of weld microstructure at the quench interface (arrows), Heat 1.

Ferrite numbers were obtained from all metallographic specimens with a Magne-Gage. Two areas on each sample were analysed: the vicinity of the quench interface, and regions far removed from this interface. Twenty readings were obtained from each region.

3. Results and discussion

3.1. Metallographic studies and analyses

Figs 3 and 4 are optical photomicrographs of the water-quench interfaces from specimens of Heats 1 and 2, respectively. The actual solid–liquid interface positions at the instant of quenching are marked by the set of arrows in each figure. The finer dendrite size to the right of the arrows is indicative of the increased cooling rate caused by the water quench. The rapid thermal shrinkage experienced by these welds resulted in the formation of intergranular hot cracks, as can be seen in each figure. CF-8M alloys undergoing this sequence of solidification (A–F) are known [2–6] to be susceptible to solidification hot cracking. In particular, these two alloys [5] are known to have a high propensity towards weld metal hot cracking. Other alloys which solidified via the F–A sequence and were subjected to the same water quenching test did not exhibit hot cracking [32].

TABLE III Cr and Ni equivalents

Heat No.		Delong Eq.*	Hammar Eq.†	Hull Eq.‡	PSM§	OSM¶
1	Cr_{eq}	23.00	24.07	23.22	A–F	A–F
	Ni_{eq}	17.89	16.89	17.12		
	Cr_{eq}/Ni_{eq}	1.29	1.42	1.36		
2	Cr_{eq}	22.15	22.99	21.56	A–F	A–F
	Ni_{eq}	17.10	15.71	15.96		
	Cr_{eq}/Ni_{eq}	1.30	1.46	1.35		

*Cr_{eq} = wt% Cr + wt% Mo + 1.5 wt% Si + 0.5 wt% Nb

Ni_{eq} = wt% Ni + 30(wt% C + wt% N) + 0.5 wt% Mn

†Cr_{eq} = wt% Cr + 1.37 wt% Mo + 1.5 wt% Si + 2 wt% Nb + 3 wt% Ti

Ni_{eq} = wt% Ni + 22 wt% C + 14.2 wt% N + wt% Cu + 0.31 wt% Mn

§Cr_{eq} = wt% Cr + 1.21 wt% Mo + 2.27 wt% V + 2.48 wt% Al + 2.20 wt% Ti + 0.48 wt% Si + 0.14 wt% Nb + 0.72 wt% W + 0.21 wt% Ta

Ni_{eq} = wt% Ni + 24.5 wt% C + 18.4 wt% N + 0.44 wt% Cu + 0.41 wt% Co + 0.11 wt% Mn-0.0086 (wt% Mn)^2

§PSM, predicted solidification mode.

¶OSM, observed solidification mode.

From the alloy chemistry, both an estimate of the amount of room-temperature ferrite observed in the microstructure and the solidification sequence may be predicted (under normal arc welding conditions) by using the appropriate "equivalent" definitions. Chromium and nickel equivalents defined by Delong [9], Hammar and Svensson [14], and Hull [26] were calculated for the two alloys. Table III lists the equivalent definitions used, the chromium and nickel equivalents calculated from each definition, the Cr_{eq}/Ni_{eq} ratios, and the solidification sequence predicted by Suutala [15] from these Cr_{eq}/Ni_{eq} ratios. Table IV lists the predicted amount of room-temperature ferrite from the Delong Diagram [9] and the amounts of ferrite measured with a Magne-Gage both in the vicinity of the quench interface and back from the interface in the bulk microstructure.

The predicted and measured values of ferrite number in the bulk microstructure were in reasonable agreement in the case of Heat 1, whereas Heat 2 was found to contain substantially less ferrite than that predicted by the Delong Diagram. The accuracy of the Delong Diagram has been reported [9] to be ±3 ferrite numbers. For a given equivalent definition, the Cr_{eq}/Ni_{eq} ratios of the two alloys listed in Table III are virtually identical, suggesting both a similarity in the solidification sequence and room-temperature ferrite content. The lack of consistency between the calculated Cr_{eq}/Ni_{eq} ratios and the measured ferrite numbers suggests that the equivalent concept may not be appropriate for differentiating the ferrite content among A–F welds as these alloys exist only over a narrow range in Cr_{eq}/Ni_{eq}.

It is reasonable to assume that the amount of ferrite in the vicinity of the interface is actually higher than that measured with the Magne-Gage. The Magne-Gage is a bulk measuring device which effectively averages the amount of ferrite present in the analysed region. In the vicinity of the quench interface, a steep thermal (and hence microstructural) gradient exists at the moment of quenching. A bulk measurement in a gradient will necessarily produce average data having a lower value than the highest value within the measured region. Fig. 5 is a scanning electron micrograph of the quench interface area in Heat 2. A heavy band of eutectic-ferrite (δ_{eu}) can be seen adjacent to the water-quench interface. Away from the interface (upper left), the amount of eutectic ferrite decreases, consistent with the Magne-Gage data.

The phenomenon of ferrite transformation to austenite in F–A type welds has been commonly observed by other investigators. Arata *et al.* [7] suggested that a large fraction of the microstructure ($\geqslant 75\%$) at the solidus temperature was ferrite in many commercial (F–A type) 304 stainless steels and that the 5 to 10% volume fraction of ferrite observed at room temperature was the result of incomplete transformation during cooling of the weld metal to ambient temperature. Similar conclusions on F–A type alloys have been suggested by others, either directly via the directional solidification and quench experiments [33] or via indirect methods such as isothermal [34] or non-isothermal [35] heat treatments of unwelded specimens at temperatures just below the solidus, or long-term isothermal heat treatments of F–A type welds at intermediate temperatures (750 to 1050° C) [36].

TABLE IV Magne-Gage ferrite numbers

Heat number	Predicted	Near quench interface	Bulk microstructure
1	2.5	3.5 ± 0.2*	3.2 ± 0.3
2	3.0	0.6 ± 0.1	0.2 ± 0.1

*Two standard deviations based upon 20 readings each.

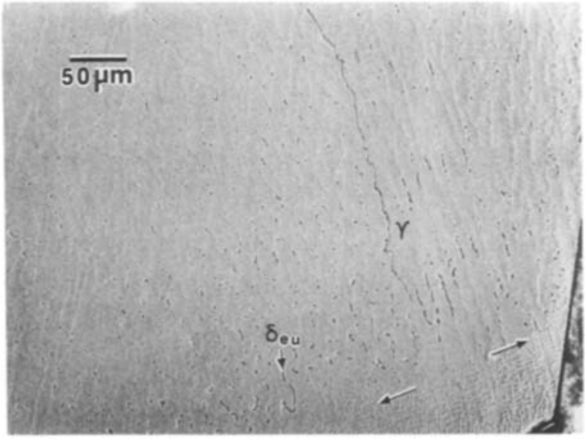

Figure 5 Secondary electron image of band of eutectic ferrite adjacent to quench interface, Heat 2.

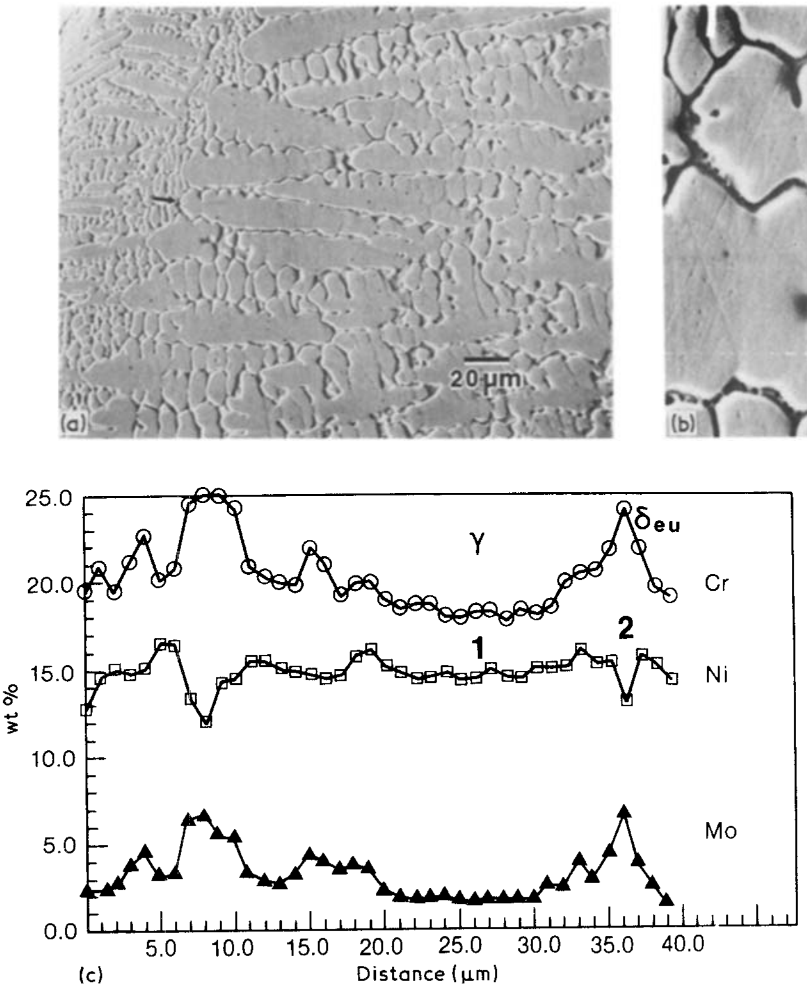

Figure 6 (a) Secondary electron image at quench interface, Heat 1. (b) Higher magnification image of analysis area in (a) showing electron microprobe profiling path (line) and position of eutectic ferrite (δ_{eu}). (c) Electron microprobe profile (chromium, nickel, molybdenum) along path identified in (b).

3.2. Electron microprobe studies and analyses

Figs 6a and b show a region at the quench interface of a Heat 1 weld that was examined with the electron microprobe. A large primary austenite dendrite can be seen in the middle-left of Fig. 6a (arrow). The electron microprobe profile (black line) was taken across the dendrite core (Area 1) and included regions of eutectic ferrite (Area 2). The profile shown in Fig. 6c reveals the pattern of microsegregation associated with solidification. The austenite dendrite is lean in chromium and molybdenum relative to the eutectic-ferrite. In addition, the segregation profile indicates that all the alloying elements (chromium, nickel, molybdenum) are partitioned to the liquid phase during solidification. It is interesting to note the extent of molybdenum segregation resulting from solidification. The highest molybdenum concentration in the eutectic ferrite just below the solidus is approximately 6.8 wt %, as measured by the electron microprobe. The nickel and chromium concentrations at this point are approximately 12.2 and 25.0 wt %, respectively. The chromium, nickel and molybdenum concentrations in the first solid to form (the core of the austenite dendrite) are approximately 17.8, 14.4, and 1.7 wt %, respectively.

Figs 7a and b show the quench interface region in Heat 2. Fig. 7b shows the path analysed by the electron microprobe, crossing a primary austenite dendrite in a similar manner as was done for Heat 1 (with Area 1 being the dendrite core and Area 2 being an interdendritic region). In this case, though, the eutectic ferrite is much less broad. Fig. 7c shows the electron microprobe profile obtained from the traverse shown in Fig. 7b. As in Heat 1, alloy depletion is observed at the primary austenite dendrite cores. The alloying element composition here is approximately 17.5 wt % Cr, 12.5 wt % Ni, and 1.5 wt % Mo. The eutectic ferrite, denoted by the drop in nickel content at the 4 µm position in Fig. 7c, has an alloying element composition of approximately 22.5 wt % Cr, 12.2 wt % Ni, and 4.6 wt % Mo. Due to the small size of the eutectic ferrite in this alloy, it is likely that the microprobe underestimates the chromium and molybdenum content of this phase while it overestimates the nickel content.

From these data, the effective distribution coefficient can be calculated for the solidification of this alloy. The effective distribution coefficient, k_e, is the ratio of the composition of the first solid to form (dendrite core) to the bulk composition. This parameter can be calculated individually for each element and represents the level of partitioning of that element between the solid and liquid phases. It is, therefore, a measure of the amount of segregation possible in a solidifying alloy. For component elements that lower the melting temperature of an alloy, k_e is less than unity, and results in the first solid to form (dendrite core) having less than the bulk composition of that particular component. Component elements that raise

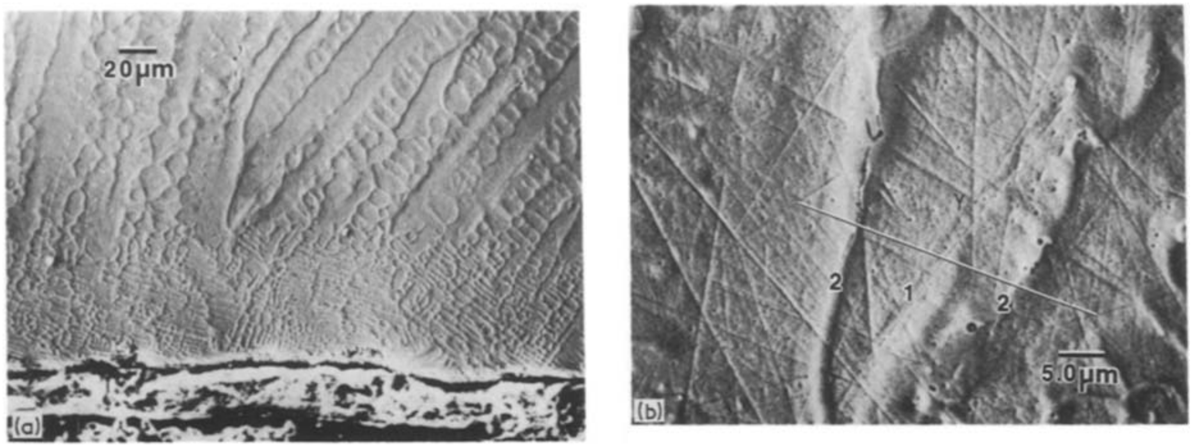

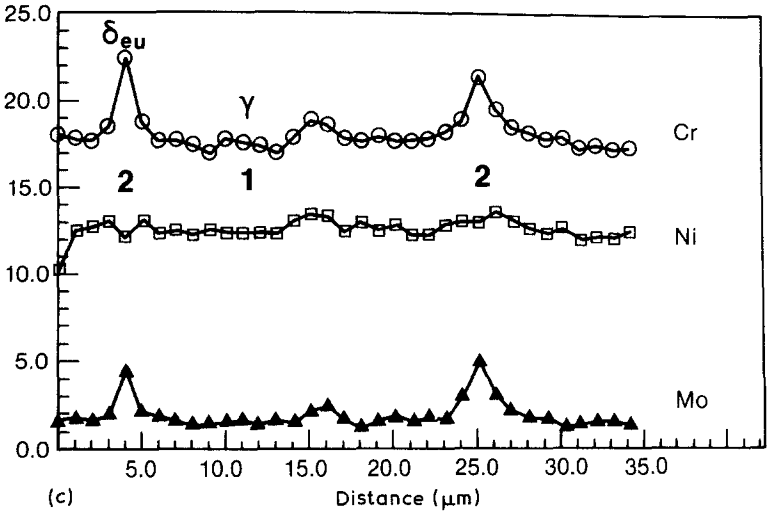

Figure 7 (a) Secondary electron image at quench interface, Heat 2. (b) Higher magnification image of analysis area in (a) showing electron microprobe profiling path (line). (c) Electron microprobe profile (chromium, nickel, molybdenum) along path identified in (b).

the melting temperature of the alloy have values of k_e greater than unity and result in the first solid to form having greater than the bulk composition of that particular component.

Table V lists the calculated k_e values for the major alloying elements in these welds. Hammar and Svensson [14] reported k_e values for nickel, chromium and molybdenum in a (A–F type) 316 stainless steel. Fredriksson [10] and Brooks *et al.* [18] have reported k_e values for nickel and chromium in A–F type alloys similar to 304 stainless steel. These are also given in Table V. The Hammar and Svensson data were obtained from electron microprobe analysis of water-quenched 30 g castings. Fredriksson's values were obtained from electron microprobe analysis of a water-quenched 4500 kg ingot and those of Brooks *et al.* were obtained by STEM/EDS analysis of GTA welds.

The values obtained in the present study for nickel and chromium are qualitatively consistent with these other data with exception of the k_e for nickel obtained by Hammar and Svensson. A k_e value for nickel greater than unity, of course, implies that the dendrite cores would have the highest nickel concentration to be found in the austenite dendrites. An examination of Figs 6c and 7c shows that this is not the case with the present alloys. These regions have the lowest nickel content found in the austenite dendrites, consistent with a $k_e < 1$, and a gradually increasing nickel concentration as the interdendritic regions are approached

TABLE V Distribution coefficients

Heat no.	Element	Bulk concentration (wt %)	Dendrite core	k_e
1	Cr	19.55	17.8	0.91
1	Ni	15.38	14.4	0.94
1	Mo	2.88	2.2	0.76
2	Cr	18.32	17.4	0.95
2	Ni	12.50	13.2	0.95
2	Mo	2.26	1.5	0.66
Hammar and Svensson [14]	Cr			0.98
	Ni			1.03
	Mo			0.81
Brooks *et al.* [18]	Cr			0.92
	Ni			0.98

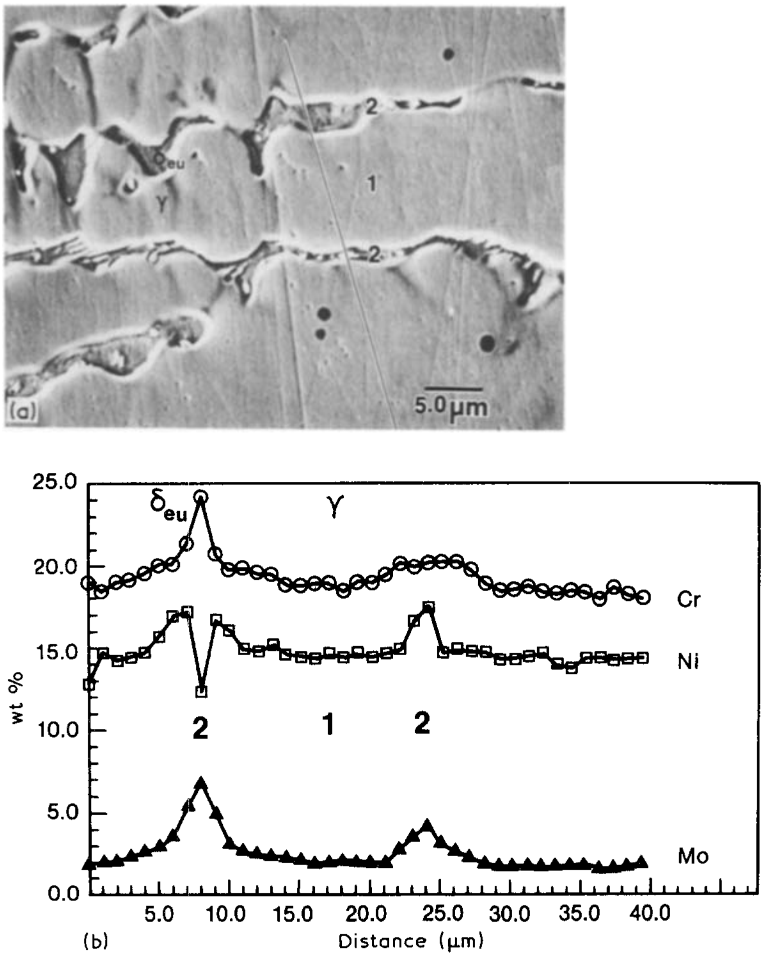

Figure 8 (a) Secondary electron image of area in Heat 1 weld far removed from the quench interface showing position of electron microprobe profile (line). (b) Electron microprobe profile (chromium, nickel, molybdenum) along path shown in (a).

(consistent with a Schiel-type solidification model [37] for $k_e < 1$). As a complete electron microprobe profile was not shown by Hammar and Svensson, further interpretation of their data is not possible.

As a final comment on the determination of k_e values, it must be remembered that they are calculated using quantities obtained from different sources. Necessarily, the dendrite core compositions must be obtained using a microanalytical technique (electron microprobe or STEM/EDS). In all cases reported, the nominal alloy chemistry was determined using a bulk analytical technique (wet chemical, spectrographic, etc.). Errors in determining each quantity affects the accuracy of k_e. For values near unity, this is even more critical and must be understood when evaluating and comparing data.

3.3. STEM/EDS studies and analyses

In order to reveal the chemical changes occurring within the eutectic ferrite as the weld cools to room temperature, it was necessary to employ the higher resolution available with STEM/EDS microanalysis. Initial experiments performed with electron microprobe gave results which were somewhat confusing, most probably due to the very fine width of the eutectic ferrite (generally < 1 μm) at lower temperatures.

An example of this is given in Fig. 8. Fig. 8a shows an area of the microstructure of Heat 1 far removed from the quench interface which was examined with the electron microprobe. Fig. 8b shows the electron microprobe profile determined from the region identified in Fig. 8a. Area 1 is the dendrite core and the areas labelled as 2 are interdendritic boundaries. Only a single data point could be centred on the eutectic ferrite (8 μm profile position). Comparing this profile to that given in Fig. 6c suggests that the chromium and molybdenum concentrations of this eutectic ferrite have decreased relative to the quench interface eutectic ferrite, while there is essentially no change in the nickel concentration. This type of electron microprobe data was not confirmed by STEM/EDS data, where a finer spatial resolution revealed the true nature of the elemental distribution within the eutectic ferrite.

It is interesting to observe in Fig. 8b the existence of an interdendritic region exhibiting white contrast (24 μm position) which does not contain eutectic ferrite. If eutectic ferrite were present, the nickel content would be lowered and the chromium content would increase still further. Note the high nickel content at this point. It is possible that the local Cr_{eq}/Ni_{eq} ratio was not high enough at this point to allow for the terminal solidification of eutectic ferrite. A second possibility is that a very small amount of eutectic ferrite did form at the end of solidification in this region, but that all of it has transformed to austenite upon subsequent cooling to room temperature. It is not possible to definitively conclude which mechanism is operative.

Figs 9 to 11 are transmission electron microscopy (TEM) micrographs and STEM/EDS profiles taken

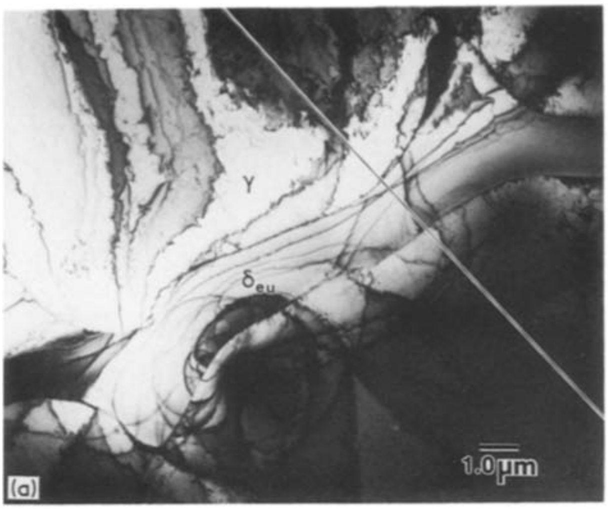

Figure 9 (a) TEM micrograph of eutectic ferrite located ≈ 1 mm from the quench interface in Heat 1 (≈ 1300° C) showing position (line) of STEM/EDS profiling path. (b) STEM/EDS composition profile (chromium, nickel, molybdenum) along path shown in (a).

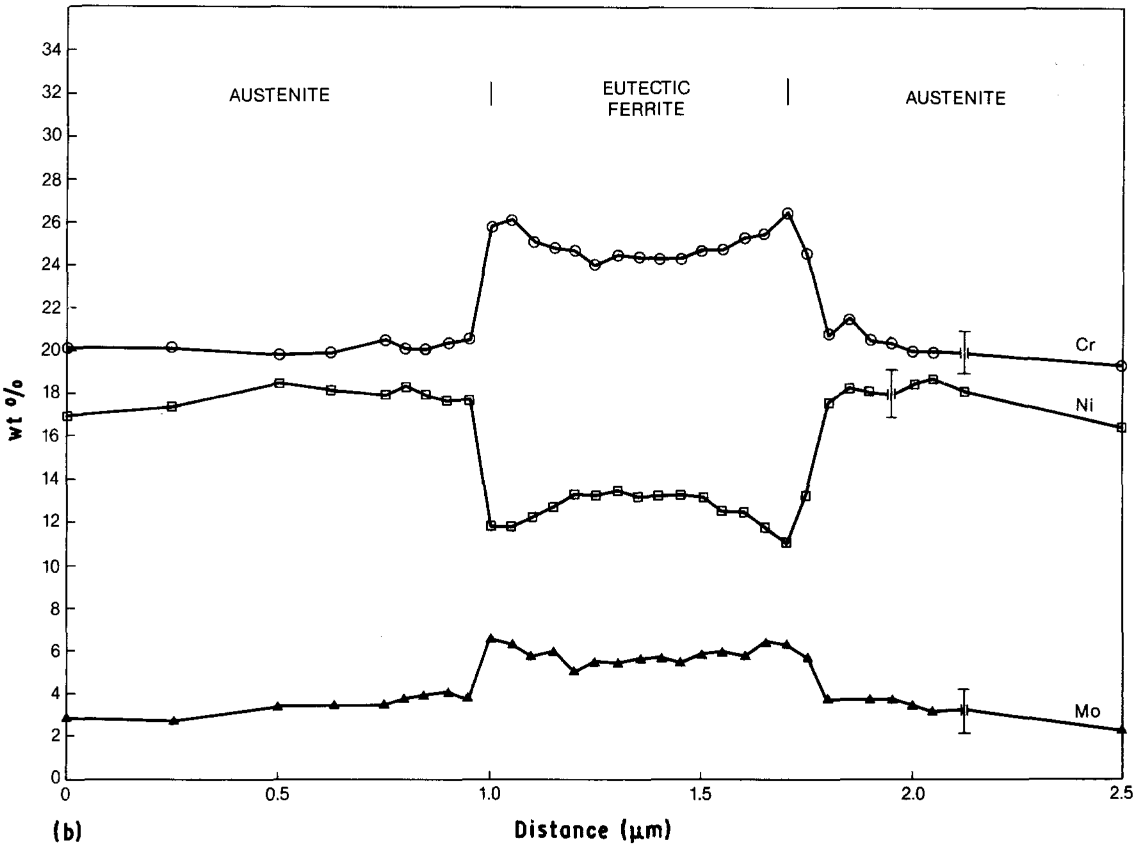

from various positions, as described in Section 2, back from the water quench interface in a Heat 1 weld. Only Heat 1 was studied with STEM/EDS techniques because this alloy had a reasonable amount of ferrite in its room-temperature microstructure on which analysis could be performed. To the authors' knowledge, these are the first reported STEM/EDS profiles taken within the eutectic ferrite phase.

Fig. 9a shows a TEM micrograph taken from a region in Heat 1 which had been at a temperature of ≈ 1300° C [6] at the instant of water quenching. This temperature is within 50° C of the solidus temperature determined by differential thermal analysis [38] of CF-8M alloys of similar composition and solidification sequence. Fig. 9b shows the STEM/EDS profile obtained from the path identified in Fig. 9a. Even quenched from this relatively high temperature, the eutectic ferrite is less than 1 μm wide.

The chromium and molybdenum concentrations within the eutectic ferrite are highest near the eutectic ferrite/austenite interface and lowest at the centre of the phase. The nickel concentration profile shows the opposite behaviour, being lowest at the interface and highest in the centre of the phase. Similar chromium and nickel STEM/EDS profiles have been observed by David *et al.* [16] in primary delta ferrite from a controlled-melt specimen of a F–A type 308 stainless steel water quenched from 1335° C.

Figs 10 and 11 show representative TEM micrographs and STEM/EDS profiles from weld metal in Heat 1 water quenched from ~ 1100 and ~ 750° C [6], respectively. A reduction in the thickness of the eutectic ferrite over these temperature ranges can be observed, especially between ~ 1300 and ~ 1100° C. Between ~ 1300 and ~ 1100° C, the average chromium concentration increased by ≈ 2 to 3 wt %, the average

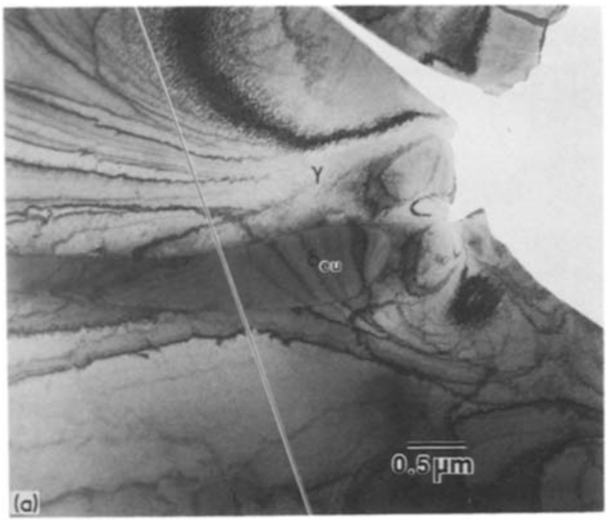

Figure 10 (a) TEM micrograph of eutectic ferrite located ≈ 4.5 mm from the quench interface in Heat 1 (≈ 1100° C) showing position (line) of STEM/EDS profiling path. (b) STEM/EDS composition profile (chromium, nickel, molybdenum) along path shown in (a).

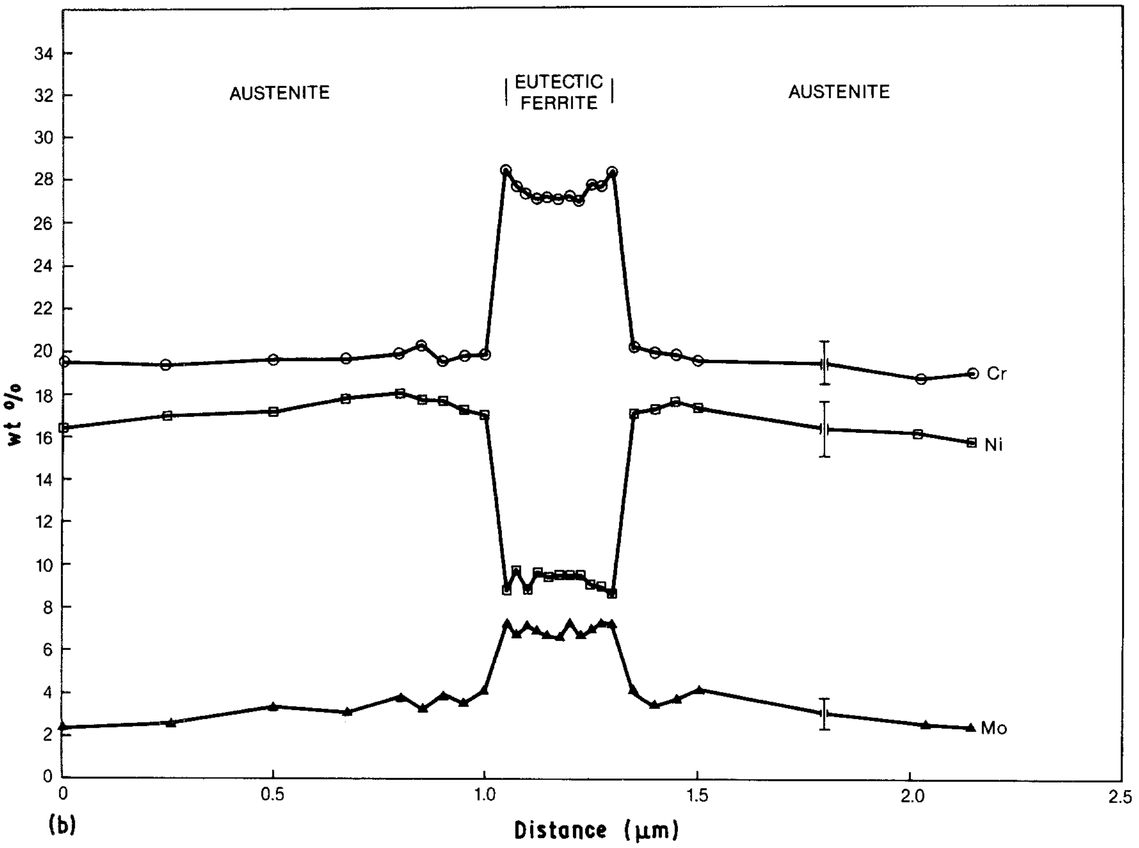

nickel concentration decreased by ~ 3 to 4 wt %, and the average molybdenum concentration increased by ≈ 1 wt %. Between ~ 1100 and ~ 750° C, the average nickel concentration decreased by ~ 1 wt % with essentially no apparent increase in either the chromium or molybdenum concentrations.

The small change in the size of the eutectic ferrite between ~ 1100 and ~ 750° C suggests that the transformation rate is markedly reduced over this temperature range. This is consistent with the lower diffusivities of the component elements in this temperature range. Diffusion data reported by Alberry and Haworth [39] for chromium and molybdenum in a ferritic matrix (diffusion in the ferrite phase is the rate determining diffusivity as this is the phase into which the austenite is growing) give diffusivities of the order of $\approx 2 \times 10^{-12}\,\mathrm{cm^2\,sec^{-1}}$ at 750° C. In this temperature range the cooling rate is of the order of $50^\circ\,\mathrm{C\,sec^{-1}}$ [6]. Assuming, then, that it takes ≈ 2 sec to cool through the 100° C temperature range surrounding 750° C, a characteristic diffusion distance, $(Dt)^{1/2}$, of ≈ 0.02 μm would be expected. As this is approximately an order of magnitude less than the diameter of the eutectic ferrite, little change in the size of the eutectic ferrite would be expected. Similar results can be shown for nickel [8, 40].

Lyman [41] has observed the same types of chromium and nickel profiles in as-welded delta ferrite from 304 (F–A type) stainless steel. Kryolainen and Porter [42] observed the same trends in F–A type 316 stainless steel for nickel and chromium. Although their profiles indicated a molybdenum increase at the delta ferrite/austenite interfaces, data scatter for molybdenum within the delta ferrite was substantial.

Farrar and Thomas [43, 44] have also performed STEM/EDS analyses on as-welded residual delta

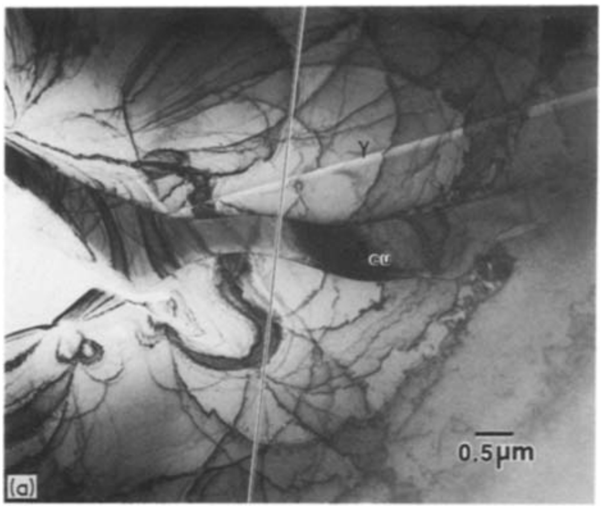

Figure 11 (a) TEM micrograph of eutectic ferrite located ≈ 20.0 mm from the quench interface in Heat 1 (≈ 750° C) showing position (line) of STEM/EDS profiling path. (b) STEM/EDS composition profile (chromium, nickel, molybdenum) along path shown in (a).

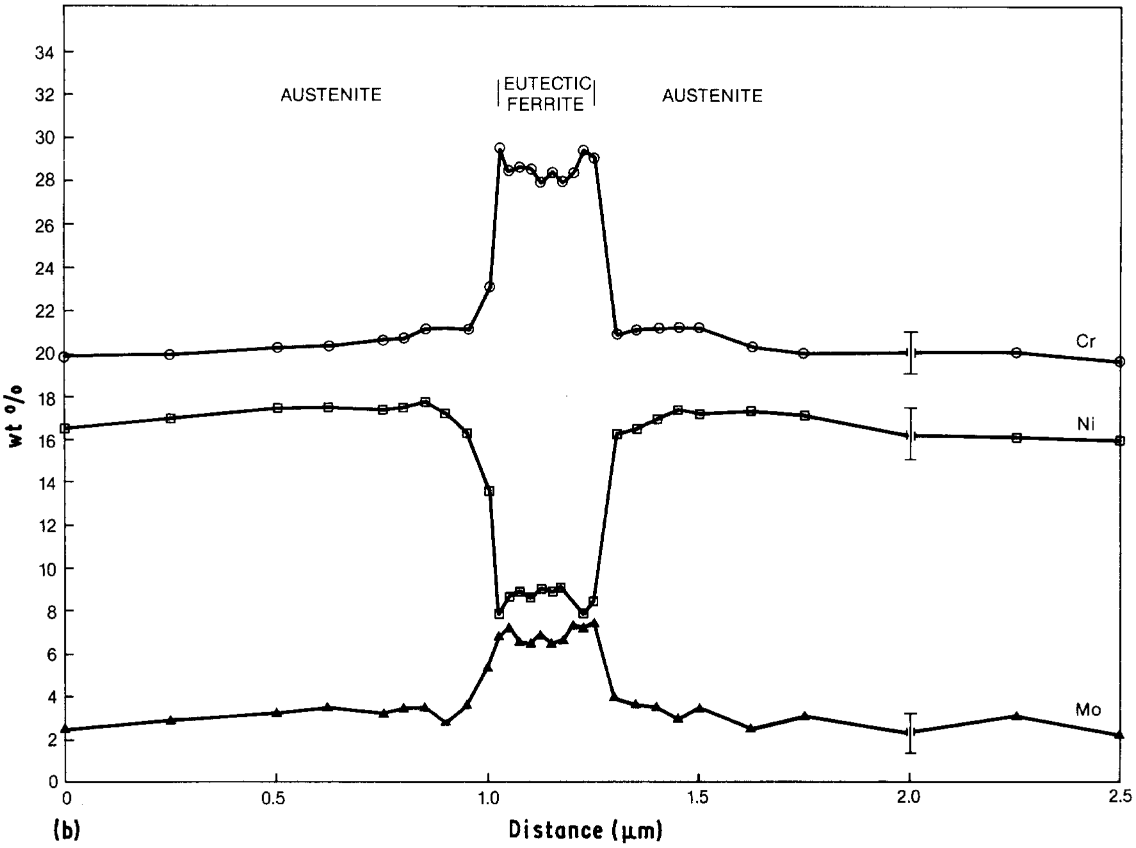

ferrite in submerged-arc-welded 316 (F–A type) stainless steel. Segregation of chromium, nickel and molybdenum is in the expected sense, but some of the fine details are not in agreement with the other reported profiles or those obtained in this study. The concave shape of the chromium profile is not observed, nor is the convex shape of the nickel profile. The molybdenum concentration is generally highest at the delta ferrite/austenite interface, but much scatter exists. Farrar and Thomas used a much coarser profiling scheme (≈ 5 analysis points per μm) than in the present study (≈ 20 analysis points per μm) which could have obscured the fine detail of the profiles. In addition, fine $M_{23}C_6$ carbide precipitation at the delta ferrite/austenite interfaces, which was sometimes observed [43], could account for the differences in some of the profile shapes.

3.4. Implications to eutectic ferrite → austenite transformation

The shapes of the compositional profiles give insight both into the transformation mechanism and partitioning behaviour of the major alloying elements during transformation. It was observed that the chromium and molybdenum concentrations within the eutectic ferrite are highest at the phase boundary and lowest at the centre of the phase. The nickel concentration shows the opposite behaviour, being the lowest at the interface and highest in the centre of the eutectic ferrite.

These observations are consistent with a diffusion-controlled transformation of eutectic-ferrite to austenite as the weld metal cools from the solidus temperature. The transformation of delta ferrite to austenite in F–A type stainless steel welds has been shown to be

TABLE VI Eutectic ferrite compositions

Element	Temperature (°C)	Interface concentration (wt %)	Range in phase
Cr	1300	27.2	27.2–25.3
	1100	29.7	29.7–28.2
	750	29.7	29.7–28.0
Ni	1300	11.6	11.6–14.1
	1100	9.1	9.1–10.3
	750	7.8	7.8–9.0
Mo	1300	6.9	6.9–5.3
	1100	7.6	7.6–6.9
	750	7.6	7.6–6.5

volume diffusion-controlled [4, 8]. The shapes of the chromium and nickel profiles within the remnants of the primary delta-ferrite dendrites were explained by Cieslak *et al.* [4] using pseudo-binary sections of the Fe–Cr–Ni ternary phase diagram.

The transformation of eutectic ferrite to austenite is consistent with this earlier model [4]. As the temperature falls from the solidus, the eutectic ferrite becomes increasingly unstable. Its transformation to austenite is governed by tie-line equilibrium considerations, at least at the interface between phases. Homogenization of the eutectic ferrite at even the highest temperatures cannot occur instantaneously. Hence, diffusion gradients are set up in the eutectic ferrite which indicate the flux directions of the component elements. The elements which stabilize the eutectic ferrite (chromium, molybdenum) are retained (diffusion gradient toward the centre of the eutectic ferrite) within an ever decreasing amount of this phase while nickel (an austenite stabilizing element) is rejected from the eutectic ferrite (diffusion gradient away from the centre of the eutectic ferrite). This causes the overall eutectic ferrite composition to be modified toward higher chromium and molybdenum concentrations and lower nickel concentration, completely analogous to the chemistry modifications occurring during the transformation of primary delta ferrite to austenite.

Table VI lists the interfacial concentrations and range of concentration of the major alloying elements found in the eutectic ferrite at the various estimated temperatures. The data indicate that the eutectic-ferrite solvus slopes toward increasing chromium and molybdenum and away from higher nickel content as the temperature decreases. The data also indicate that the eutectic ferrite solvus is close to vertical along the chromium and molybdenum isopleths (29.7 and 7.6 wt %, respectively) below a temperature of approximately 1100° C. That is, the interface concentration of these elements does not change in this temperature range. The eutectic ferrite solvus continues to slope away from the higher nickel isopleths in the temperature range 1100 to 750° C as the interface nickel concentration continues to fall.

4. Conclusions

The following conclusions were drawn from the analysis of results reported in this paper.

1. The transformation of eutectic ferrite to austenite during weld metal cooling is consistent with a volume diffusion-control mechanism.
2. During transformation (as the temperature falls), the chromium and molybdenum contents of the eutectic ferrite increase and the nickel content decreases.
3. In the temperature range 1300 to 1100° C, the eutectic ferrite solvus slopes toward higher chromium and molybdenum concentrations and away from higher nickel concentrations.
4. The position of the eutectic ferrite solvus relative to the chromium and molybdenum isopleths remains essentially unchanged over the temperature range 1100 to 750° C, whereas the solvus continues to move toward lower nickel contents over this same temperature range.
5. The calculated values of the effective distribution coefficients, k_e (< 1 for all major alloying elements), indicates that each of these elements will tend to segregate to interdendritic regions during the A–F solidification sequence.
6. The calculated Cr_{eq}/Ni_{eq} ratios successfully predicted the solidification sequence of both alloy weld metals according to the criterion of Suutala [15], but did not predict the relative amounts of eutectic ferrite correctly.

Acknowledgements

The authors would like to thank Dr E. L. Hall and A. M. Ritter for helpful technical discussions.

References

1. "Metals Handbook", 8th Edn, Vol. 1 (American Society for Metals, Metals Park, Ohio, 1961) p. 433.
2. A. M. RITTER, M. J. CIESLAK and W. F. SAVAGE, *Met. Trans. A* **14A** (1983) 37.
3. M. J. CIESLAK, MS thesis, Rensselaer Polytechnic Institute, Troy, New York, (1979).
4. M. J. CIESLAK, A. M. RITTER and W. F. SAVAGE, *Weld. J.* **6** (1982) 1-s.
5. M. J. CIESLAK and W. F. SAVAGE, *ibid.* **59** (1980) 136-s.
6. M. J. CIESLAK, A. M. RITTER and W. F. SAVAGE, *ibid.* **63** (1984) 133-s.
7. Y. ARATA, F. MATSUDA and S. KATAYAMA, *Trans. JWRI* **5** (1976) 35.
8. G. L. LEONE and H. W. KERR, *Weld. J.* **61** (1982) 13-s.
9. W. T. DELONG, *ibid.* **53** (1974) 273-s.
10. H. FREDRIKSSON, *Met. Trans.* **3** (1972) 2989.
11. J. C. LIPPOLD and W. F. SAVAGE, *Weld. J.* **59** (1980) 48-s.
12. N. SUUTALA, *Met. Trans. A* **14A** (1983) 191.
13. N. SUUTALA and T. MOISIO, "Solidification Technology in the Foundry and Casthouse" (The Metals Society, London, 1980) Session IVA, p. 1.
14. O. HAMMAR and U. SVENSSON, "Solidification and Casting of Metals" (The Metals Society, London, 1979) p. 401.
15. N. SUUTALA, *Met. Trans. A* **13A** (1982) 2121.
16. S. A. DAVID, G. M. GOODWIN and D. N. BRASKI, *Weld. J.* **58** (1979) 330-s.
17. N. SUUTALA, T. TAKALO and T. MOISIO, *Met. Trans. A* **10A** (1979) 512.
18. J. A. BROOKS, J. C. WILLIAMS and A. W. THOMPSON, *ibid.* **14A** (1983) 23.
19. T. TAKALO, N. SUUTALA and T. MOISIO, *ibid.* **10A** (1979) 1173.
20. N. SUUTALA, T. TAKALO and T. MOISIO, *ibid.* **11A** (1980) 717.
21. V. KUJANPAA and T. MOISIO, "Solidification Technol-

ogy in the Foundry and Casthouse" (The Metals Society, London, 1980) Session IVB, p. 1.

22. M. J. CIESLAK and W. F. SAVAGE, *Weld. J.* **60** (1981) 131-s.
23. S. A. DAVID, *ibid.* **60** (1981) 63-s.
24. J. C. LIPPOLD and W. F. SAVAGE, *ibid.* **61** (1982) 388-s.
25. N. SUUTALA, T. TAKALO and T. MOISIO, *ibid.* **60** (1981) 92-s.
26. F. C. HULL, *ibid.* **46** (1967) 399-s.
27. A. SCHAEFLER, *Metal Progress* **56** (1949) 680.
28. "Annual Book of ASTM Standards", Vol. 3.03 (American Society for Testing Materials, Philadelphia, Pennsylvania, 1983) p. 523.
29. J. W. COLBY, "Advances in X-Ray Analysis", edited by J. B. Newkirk, G. R. Mallett and H. G. Pfeiffer, Vol. 11 (Plenum, New York, 1968) p. 287.
30. G. CLIFF, G. W. LORIMER, "Proceedings of the Fifth European Conference on Electron Microscopy" (Institute of Physics, London, 1972) p. 140.
31. J. I. GOLDSTEIN, J. L. COSTLEY, G. W. LORIMER, S. J. B. REED, *Scanning Electron Microscopy* **1** (1977) 315.
32. N. LEWIS, MS thesis, Rensselaer Polytechnic Institute, Troy, New York (1983).
33. K. H. CARDER, MS thesis, Iowa State University Ames Laboratory, Ames, Iowa, (1986).
34. A. M. RITTER, M. F. HENRY and W. F. SAVAGE, *Met. Trans. A* **15A** (1984) 1339.
35. J. A. BROOKS, A. W. THOMPSON and J. C. WILLIAMS, *Weld. J.* **63** (1984) 71-s.
36. J. M. VITEK and S. A. DAVID, "Trends in Welding Research in the United States" (American Society for Metals, Metals Park, Ohio, 1982) p. 243.
37. E. SCHEIL, *Z. Metallkde* **34** (1942) 70.
38. M. J. CIESLAK and W. F. SAVAGE, *Weld. J.* **64** (1985) 119-s.
39. P. J. ALBERRY and C. W. HAWORTH, *Metal. Sci.* **8** (1974) 407.
40. D. B. MOHARIL, I. JIN and G. R. PURDY, *Met. Trans.* **5** (1974) 59.
41. C. E. LYMAN, *Weld. J.* **58** (1979) 189-s.
42. A. KYROLAINEN, D. A. PORTER, in "Introduction to the Physical Metallurgy of Welding", by Kenneth Easterling (Butterworths, 1983) p. 88.
43. R. A. FARRAR, *J. Mater. Sci.* **20** (1985) 4215.
44. R. A. FARRAR, R. G. THOMAS, *ibid.* **18** (1983) 3461.

Received 27 August 1986
and accepted 15 January 1987